Supporting Information

Anthraquinone-intercalated V_2O_5 with Al^{3+} for superior zinc–ion battery: reversible transformation between disorder and order

Kai Li, Jia Lv, Tong Cao, Yun Gong* and Da Liang Zhang*

College of Chemistry and Chemical Engineering, Chongqing University, Chongqing 401331, P. R. China. E-mail: gongyun7211@cqu.edu.cn; Tel:+86 023 65678932 (Y. Gong); Daliang.zhang@cqu.edu.cn (D. L. Zhang)

Experimental section

Materials

Vanadium pentoxide (V_2O_5) and $Al_2(SO_4)_3 \cdot 18H_2O$ were purchased from Chengdu Cologne Chemical Co. Ltd. 1, 8-dihydroxyanthraquinone (1, 8-DHAQ) and graphite were obtained from Aladdin Biochemical Technology Co. Ltd. Hydrogen peroxide (H_2O_2, 30 %) was obtained from Shanghai Myrell Chemical Technology Co. Ltd. All reagents were of analytical grade and used directly. Zn foil (thickness: 0.1 mm) was obtained from Runde Metal Materials Co., Ltd. Carbon cloth (W0S1009, thickness: 0.1 mm) was purchased from Suzhou Sinero Technology Co. Ltd. Glass fiber membrane (Grade GF/C) was obtained from Whatman Company.

Syntheses of AQ-VO and $V_2O_5 \cdot nH_2O$

AQ-VO was synthesized by a one-step hydrothermal method. Firstly, 50 mg V_2O_5 was dissolved into the mixed solution of 5 mL deionized water and 1 mL H_2O_2 (30 %) under ultrasonic treatment to obtain solution A. Meanwhile, 50 mg 1, 8-DHAQ was dispersed in 5 mL absolute ethanol under ultrasonic treatment to obtain part B. Afterwards, mix solution A and part B under ultrasonic treatment, then the mixture was sealed in a 15 mL autoclave and maintained at 150 ^{o}C for 12 h. The precipitation was collected by centrifugation and washed with deionized water several times, finally

frozen and underwent a freeze -drying process. $V_2O_5 \cdot nH_2O$ was synthesized under the same condition but in the absence of 1, 8-DHAQ.

Material characterizations

Powder X-ray diffractometer (XRD) (PANalytical X'pert Pro MPD) with Cu Kα radiation (λ = 1.54056 Å) was utilized to obtain crystalline structures of the samples. Fourier transform infrared spectra (IR) were performed on IR spectrometer (IRTracer-100). Thermogravimetric (TG) curves were measured on a METTLER TOLEDO TGA2 analyzer from room temperature to 800 ℃ in N_2 atmosphere. X-ray photoelectron spectroscopy (XPS) was carried out on an ESCALAB 250 analyzer to detect the chemical states of elements on the surface. Electron paramagnetic resonance (EPR) spectroscopy was performed using an EPR (BRUKE EMXPLUS) with the center field of 3510 G and sweep width of 100 G. Scanning electron microscopy (SEM) and energy-dispersive X-ray spectroscopy (EDS) as well as elemental mapping images of the samples were collected by Thermo Fisher (Quattro S) instrument equipped with an EDS (AMETEK) analyzer. Transmission electron microscopy (TEM), high resolution TEM (HRTEM) and selected area electron diffraction (SAED) patterns were performed on a Thermo Fisher Talos F200s apparatus with an EDS (Super-X) analyzer.

Electrochemical measurements

The fabrication of the cathode was as follows: AQ-VO or $V_2O_5 \cdot nH_2O$ was mixed with acetylene black (AB), graphite and polyvinylidene fluoride (PVDF) with a mass ratio of 5: 2: 2: 1 in N-methyl pyrrolidone (NMP) solvent. The obtained slurry was evenly coated onto the carbon cloth (CC) (diameter: 12 mm, thickness: ~ 0.35 mm) with a doctor blade and dried at 120 ^oC in vacuum for at least 6 h. The loading mass of the active material is in the range of 2.6 ~ 3.5 mg cm^{-2}. CR2032 coin cells were

assembled in air with Zn foil (thickness: 0.1 mm) and glass fiber (Whatman GF/C, thickness: 260 μm) used as the anode and separator, respectively, in which 3 M $Zn(CF_3SO_3)_2$ or the mixture of 2.8 M $Zn(CF_3SO_3)_2$ and 0.1 M $Al_2(SO_4)_3$ aqueous solution (~ 100 μL) was used as the electrolyte. Before the electrochemical tests, the coin cells were aged 8 h at room temperature of 25 ^oC. And all the electrochemical tests were also carried out at room temperature (25 ^oC).

CHI660E electrochemical workstation (Shanghai Chenhua, China) was employed to obtain cyclic voltammetry (CV) and electrochemical impedance spectroscopy (EIS). And EIS was performed with an AC amplitude voltage of 5 mV in the frequency range of 0.01 Hz ~ 100 kHz. LAND CT2001A (5V/10 mA or 5 V/100 mA) battery testing system was used to get galvanostatic charge/discharge (GCD) and galvanostatic intermittent titration technique (GITT) curves with the voltage range of 0.2 to 1.6 V. During GITT test, the cell was discharged and charged at 0.05 A g^{-1} for 15 min, and then relaxed for 30 min to allow the voltage to reach equilibrium. This process was repeatedly applied until the charge/discharge voltage reached 0.2/1.6 V.

Density functional theory (DFT) calculations

DFT calculations were conducted to investigate the diffusion of Zn^{2+} in AQ-VO via the Vienna ab initio simulation package (VASP).[1] The projector augmented wave (PAW) method with Perdew–Burke–Ernzerhof (PBE) functional was implemented in electronic structure calculations.[2] The cut-off energy of 500 eV and Monkhorst–Pack *k*-point mesh of 3 × 3 × 3 grid were adopted. The convergence threshold for the force and energy were set to 0.01 eV $Å^{-1}$ and 10^{-5} eV, respectively. The binding energy (ΔE) for the intercalation of Zn^{2+} into the inner channel of AQ-VO was calculated based on the formula $\Delta E = [E\text{ (AQ-VO / }x\text{ Zn) - }E\text{ (AQ-VO) - }x\ E\text{ (Zn)}] / x,$ where E(AQ-VO / x Zn) is the total energy after Zn^{2+} intercalated into AQ-VO, whereas E(AQ-VO) is the energy

of the individual AQ-VO. And *E* (Zn) is the energy per Zn atom (hcp).

An unit cell of AQ-VO was utilized for the simulation of the migration path and energy barrier of Zn^{2+} via the climbing-image nudged elastic band (cNEB) method.[3]

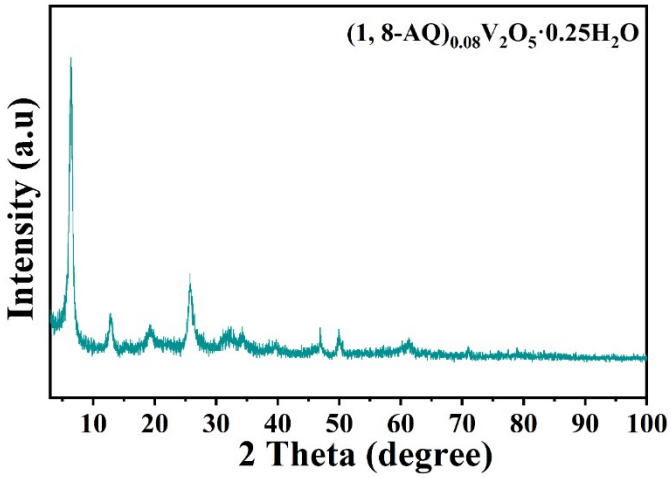

Fig. S1 XRD pattern of the $(1, 8\text{-AQ})_{0.08}V_2O_5{\cdot}0.25H_2O$ sample in the range of 3 ~ 100°.

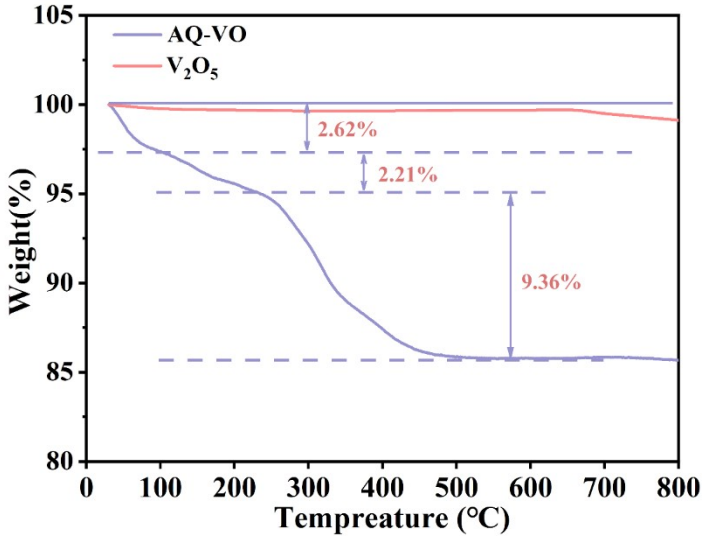

Fig. S2 TG curves of AQ-VO and the commercial V_2O_5.

S1 The IR spectrum analysis of AQ-VO

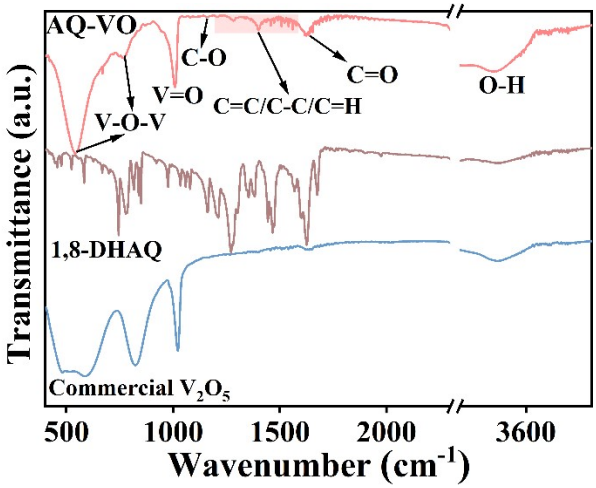

Fig. S3 IR spectra of AQ-VO.

As shown in **Fig. 1c**, The IR spectrum of AQ-VO exhibits peaks at 534 and 768 cm^{-1}, which are similar to those in V_2O_5 and can be attributed to the V-O-V bending vibrations. And the peak at ~ 1010 cm^{-1} is assigned to V=O stretching vibration.[4]

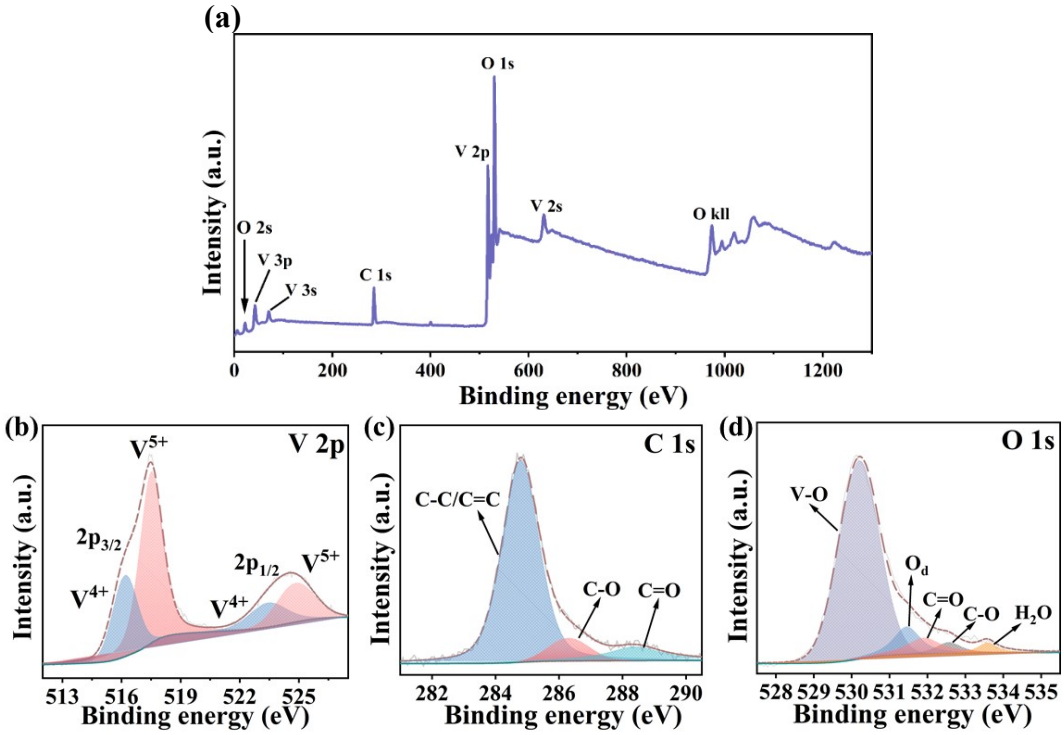

Fig. S4 The XPS spectra of AQ-VO: (**a**) survey spectrum; (**b**) V 2p, (**c**) C 2p, (**d**) O 1s.

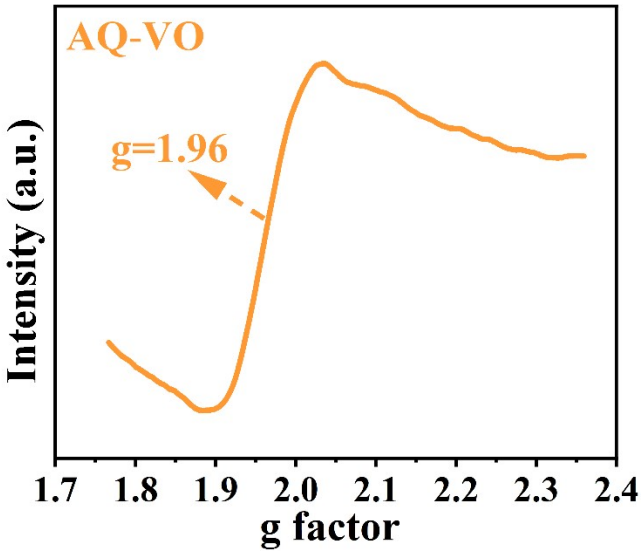

Fig. S5 EPR spectrum of AQ-VO.

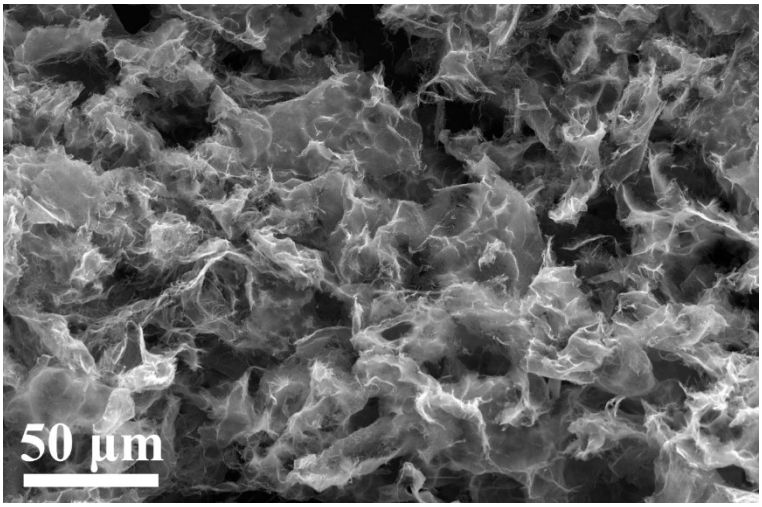

Fig. S6 SEM image of AQ-VO.

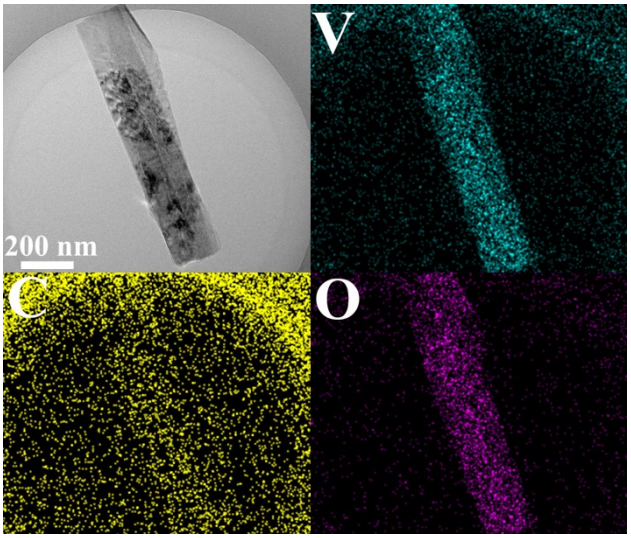

Fig. S7 TEM image and element mapping images of AQ-VO nanobelt.

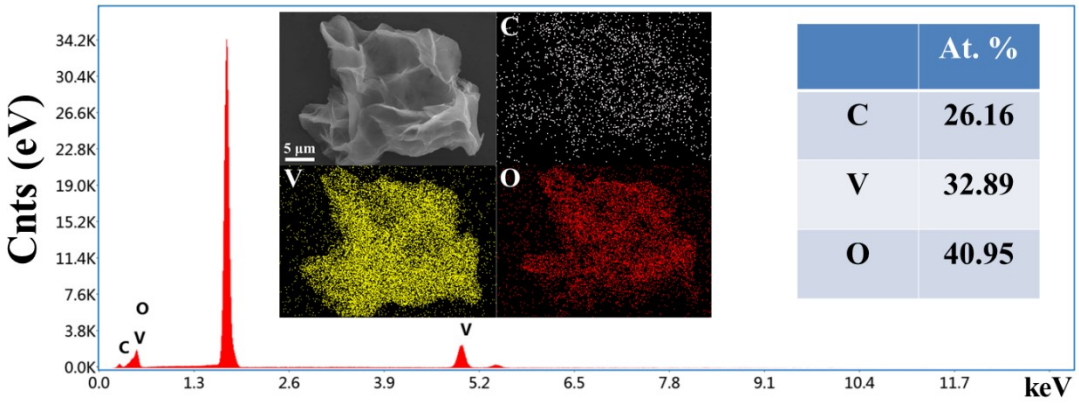

Fig. S8 EDS as well as elemental mappings of AQ-VO.

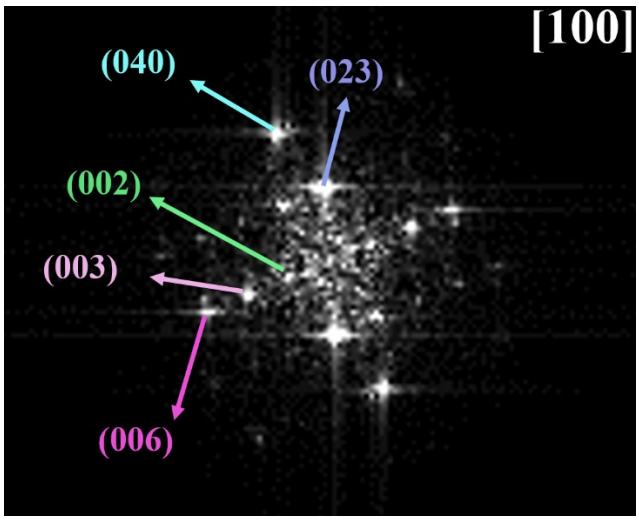

Fig. S9 FFT spectrum of AQ-VO.

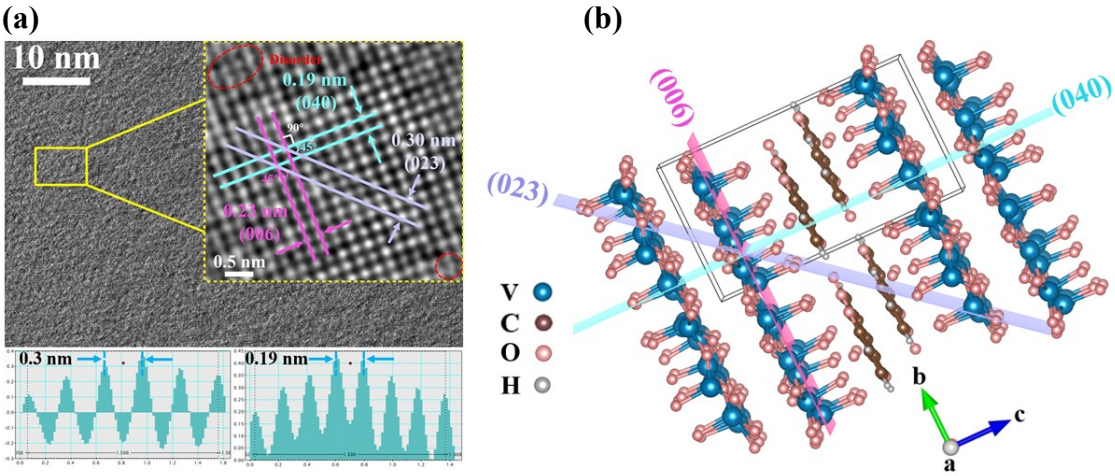

Fig. S10 (a) HRTEM images of AQ-VO; **(b)** The relative positions of the observed facets.

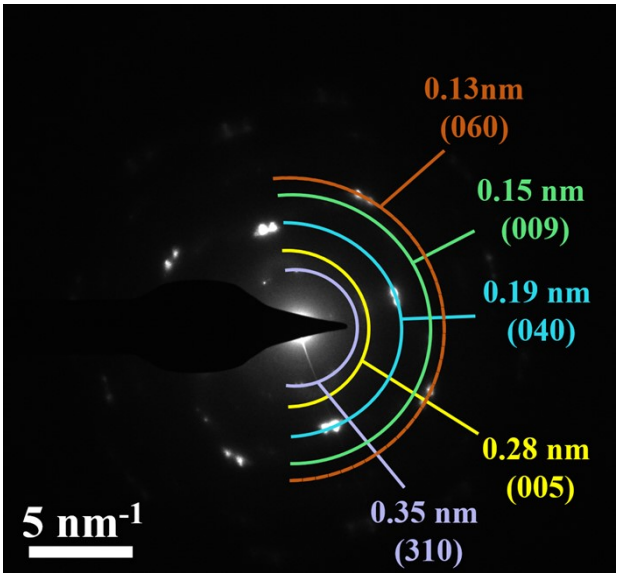

Fig. S11 SAED pattern of AQ-VO.

S2 The characterization of $V_2O_5 \cdot nH_2O$

The synthesis of $V_2O_5 \cdot nH_2O$ was similar to that of AQ-VO except in the absence of 1, 8-DHAQ. The XRD patterns of $V_2O_5 \cdot nH_2O$ and the commercial V_2O_5 are shown in **Fig. S12**. It can be seen that the commercial V_2O_5 crystallizes in orthorhombic crystal system (JCPDS No. 72-0433) with the strongest diffraction peak observed at 20.3 °. After hydrothermal reaction, the obtained $V_2O_5 \cdot nH_2O$ shows the strongest diffraction peak at 6.6 °, suggesting the interlayer spacing is expanded to be ~13.2 Å due to the intercalation of H_2O.

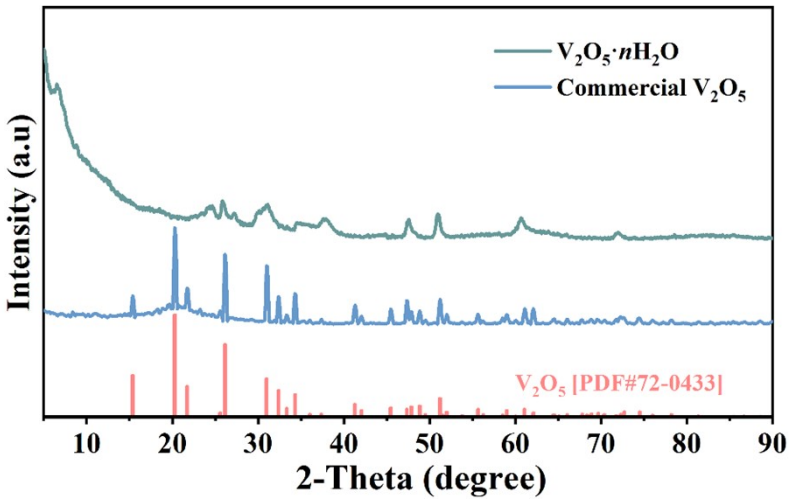

Fig. S12 XRD patterns of $V_2O_5 \cdot nH_2O$, the commercial V_2O_5 and the standard profile.

Table S1 The comparison of the electrochemical performances of AQ-VO and other vanadium-based materials.

Material	**Specific capacity**	**Cycle number**	**Capacity retention**	**Reference**
BVO-3	321 mAh g^{-1} at 0.1 A g^{-1}	2000 (5 A g^{-1})	95.6 %	[5]
δ-$Ni_{0.25}V_2O_5$· nH_2O	402 mAh g^{-1} at 0.2 A g^{-1}	1200 (5.0 A g^{-1})	98.0 %	[6]
MnVO	415 mAh g^{-1} at 0.05 A g^{-1}	2000 (4.0 A g^{-1})	92.0 %	[7]
$Li_xV_2O_5$ ·n H_2O	470 mAh g^{-1} at 0.05 A g^{-1}	1000 (10.0 A g^{-1})	93.0 %	[8]
$Mg_{0.34}V_2O_5$ ·$0.84H_2O$	353 mAh g^{-1} at 0.05 A g^{-1}	2000 (5.0 A g^{-1})	97.0 %	[9]
AlVO	418 mAh g^{-1} at 0.2 A g^{-1}	1000 (5.0 A g^{-1})	90.5 %	[10]
PA-VOP	268.2 mAh g^{-1} at 0.1 A g^{-1}	2000 (5.0 A g^{-1})	92.3 %	[11]
PEDOT-NVO	356.8 mAh g^{-1} at 0.05 A g^{-1}	5000 (10.0 A g^{-1})	94.1 %	[12]
bilayer-VOP	313.6 mAh g^{-1} at 0.1 A g^{-1}	2000 (5.0 A g^{-1})	76.8 %	[13]
AQ-VO with Al^{3+}	**424.7 mAh g^{-1} at 0.2 A g^{-1}**	**1700 (1 A g^{-1}) 2800 (5 A g^{-1})**	**97.2 % 99.2 %**	**This work**

S3 The cycling performances of AQ-VO at 5 A g^{-1} in the electrolyte with and without Al^{3+}

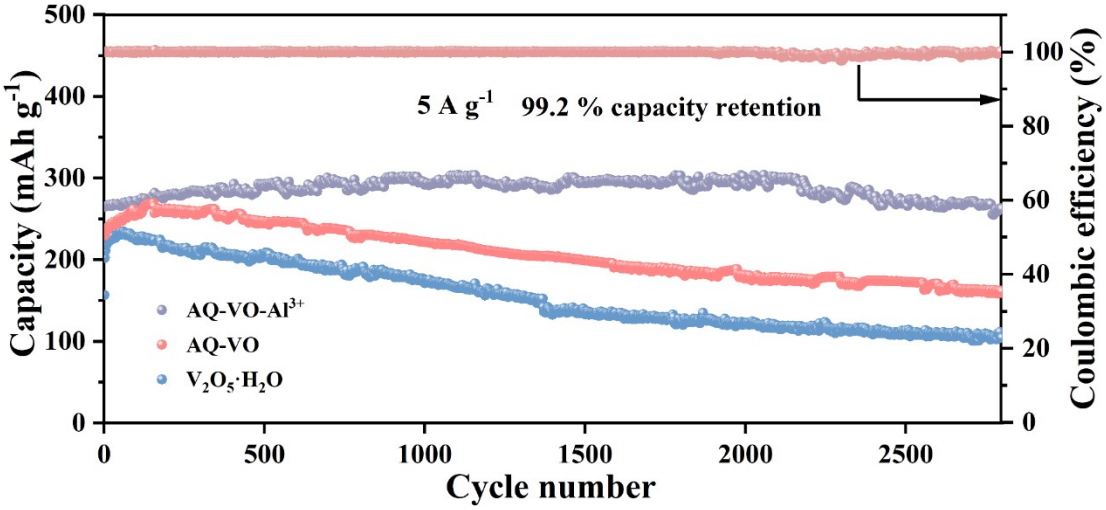

Fig. S13 The cycling performances of AQ-VO, $V_2O_5 \cdot nH_2O$ in the electrolytes with and without Al^{3+} at 5 A g^{-1}.

The long-term cycling durability of AQ-VO was further explored at a large current density of 5 A g^{-1} (**Fig. S13**). In the electrolyte with Al^{3+}, AQ-VO can maintain a high discharge capacity of 262 mAh g^{-1} over 2800 cycles with a 99.2 % of capacity retention, which is superior to many previously reported vanadium-based cathode materials in ZIBs (**Table S1**). In contrast, the capacities of AQ-VO (162 mAh g^{-1}; capacity retention: 69.2 %) and $V_2O_5 \cdot nH_2O$ (104 mAh g^{-1}; capacity retention: 53.6 %) in the absence of Al^{3+} fast fade during the cycling test at 5 A g^{-1}, further verifying the effect of dual-pillar on the cycle life of the layered vanadium oxide.

S4 Electrochemical kinetics of AQ-VO in 3 M $Zn(CF_3SO_3)_2$

The first three cyclic voltammetry (CV) curves of AQ-VO, 1, 8-DHAQ and $V_2O_5 \cdot nH_2O$ in 3 M $Zn(CF_3SO_3)_2$ at 0.1 mV s^{-1} are displayed in **Fig. S14 (a-c)**. As shown in **Fig. S14a**, it is found that the 2nd and 3rd CV curves of AQ-VO are almost overlapped, indicating the electrochemical behavior of AQ-VO tends to be stable after the 2nd cycle. And AQ-VO exhibits three pairs of distinct redox peaks at 0.98/1.01, 0.6/0.72 and

0.41/0.45 vs Zn^{2+}/Zn (**Fig. S14a**). Compared with the CVs of 1, 8-DHAQ (**Fig. S14b**) and $V_2O_5{\cdot}nH_2O$ (**Fig. S14c**), it can be concluded that the peaks at 0.41/0.45 vs Zn^{2+}/Zn in the CV of AQ-VO are ascribed to the redox of the AQ organic species, and another two pairs of peaks at 0.6/0.72 and 0.98/1.01 vs Zn^{2+}/Zn correspond to the conversion of $V^{3+} \leftrightarrow V^{4+}$ and $V^{4+} \leftrightarrow V^{5+}$, respectively.[14]

To better understand the reaction kinetics of AQ-VO in 3 M $Zn(CF_3SO_3)_2$, the CVs of AQ-VO at different scan rates were investigated (**Fig. S14d**). From 0.1 to 1.2 mV s^{-1}, the curves show similar shape at all sweep rates. Generally speaking, the relationship of the peak current (i) and scan rate (v) obeys a power law of $i = av^b$, which can be written as log (i) = b log (v) + log(a), where b represents the slope of the log(i) vs log(v) plot. Ionic diffusion controls the reaction process when the value of b is 0.5, and pseudocapacitance dominates the electrochemical process when the value of b is 1. As displayed in **Fig. S14e**, the calculated b values of peaks **1-4** marked in **Fig. S14d** are 0.82, 0.94, 0.80 and 0.97, respectively, demonstrating the coexistence of diffusion control and capacitive behavior in AQ-VO. Moreover, the capacitive and diffusion-controlled contributions can be quantified according to the formula of $i/v^{1/2} = k_1v^{1/2} + k_2$. As shown in **Fig. S14f**, the capacitive contribution of AQ-VO accounts for 86.6% of the whole capacity at 1.0 mV s^{-1}. And the capacitive contribution ratio increases from 67.2 to 89.6 % when the scan rate increases from 0.1 to 1.2 mV s^{-1} (**Fig. S14g**).

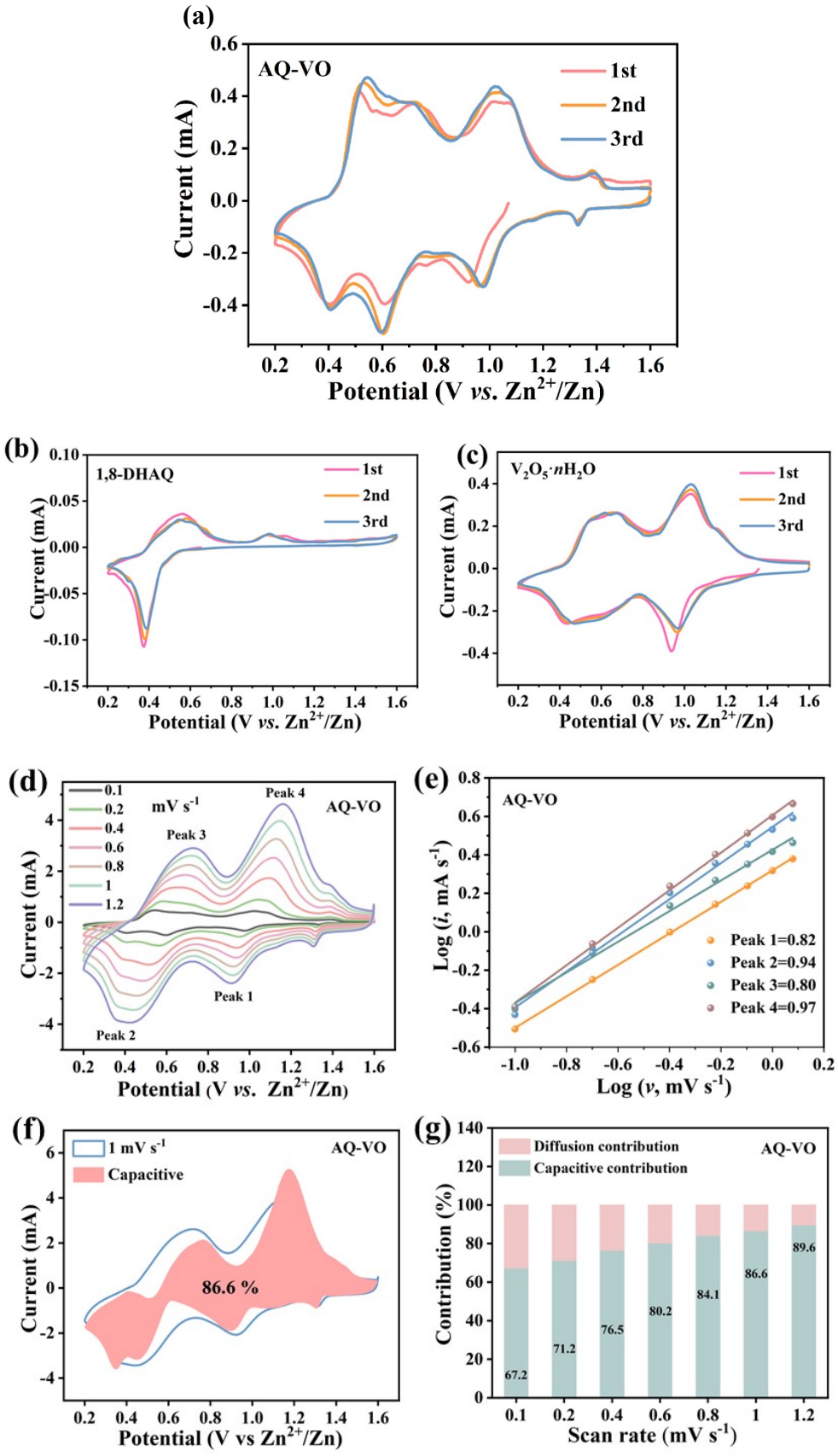
(a)
AQ-VO
1st
2nd
3rd
Current (mA)
Potential (V vs. Zn2+/Zn)
(b)
1,8-DHAQ
1st
2nd
3rd
Current (mA)
Potential (V vs. Zn2+/Zn)
(c)
V2O5·nH2O
1st
2nd
3rd
Current (mA)
Potential (V vs. Zn2+/Zn)
(d)
0.1
0.2
0.4
0.6
0.8
1
1.2
mV s-1
AQ-VO
Peak 1
Peak 2
Peak 3
Peak 4
Current (mA)
Potential (V vs. Zn2+/Zn)
(e)
AQ-VO
Peak 1=0.82
Peak 2=0.94
Peak 3=0.80
Peak 4=0.97
Log (i, mA s-1)
Log (v, mV s-1)
(f)
1 mV s-1
Capacitive
AQ-VO
86.6 %
Current (mA)
Potential (V vs Zn2+/Zn)
(g)
Diffusion contribution
Capacitive contribution
AQ-VO
67.2
71.2
76.5
80.2
84.1
86.6
89.6
Contribution (%)
Scan rate (mV s-1)

(h)

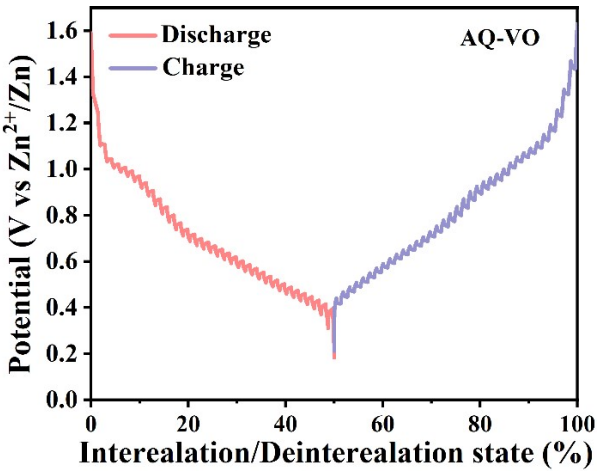
Discharge
Charge
AQ-VO
Potential (V vs Zn2+/Zn)
Interealation/Deinterealation state (%)

(i)

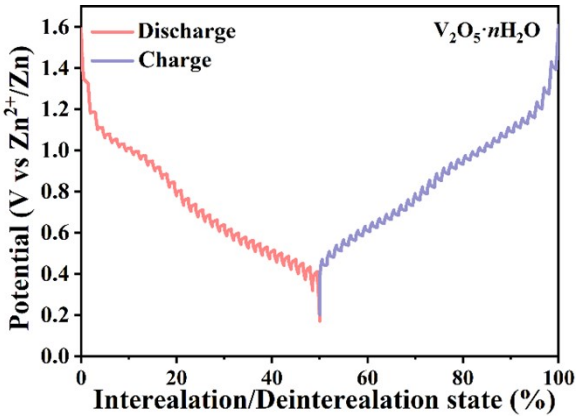
Discharge
Charge
V2O5·nH2O
Potential (V vs Zn2+/Zn)
Interealation/Deinterealation state (%)

(j)

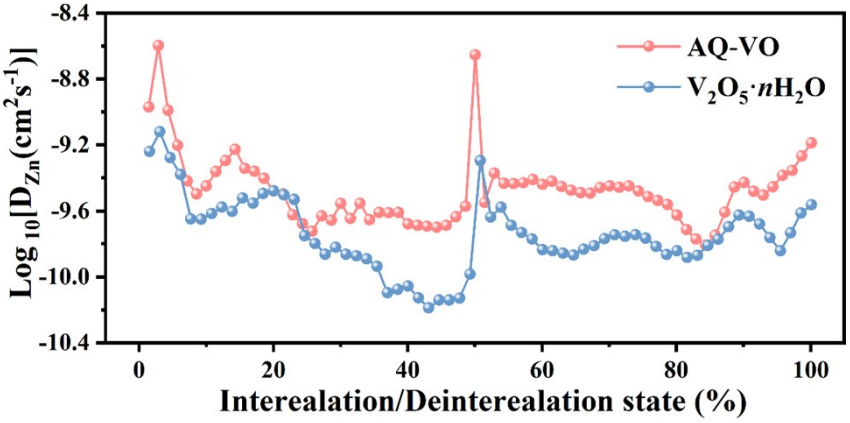
AQ-VO
V2O5·nH2O
Log10[DZn(cm2s-1)]
Interealation/Deinterealation state (%)

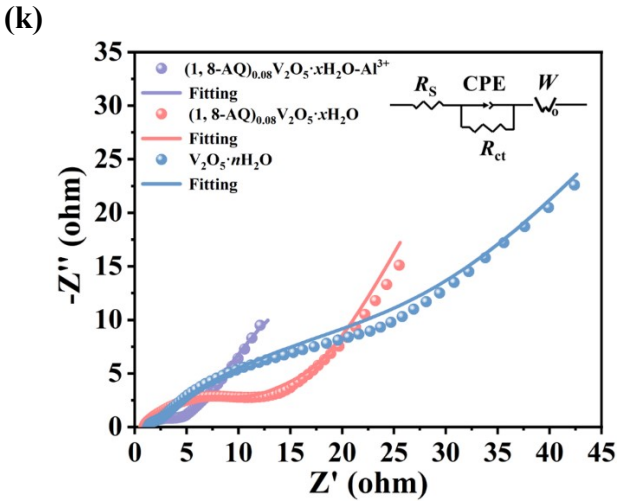

Fig. S14 The first three CVs of (**a**) AQ-VO, (**b**) 1, 8-DHAQ and (**c**) $V_2O_5{\cdot}nH_2O$ at 0.1 mV s^{-1}; (**d**) CV profiles of AQ-VO at different scan rates; (**e**) The plots of log *v* vs log *i* for peaks **1-4** in **d**; (**f**) CV of AQ-VO at 1 mV s^{-1}, highlighting the capacitive contribution; (**g**) The percentages of capacitive contribution to the total capacity in AQ-VO at different scan rates; (**h, i**) GITT profiles and (**j**) the calculated $D_{Zn^{2+}}$ of (**h**) AQ-VO and (**i**) $V_2O_5{\cdot}nH_2O$; (**k**) Nyquist plots.

Additionally, galvanostatic intermittent titration technique (GITT) was used to determine the diffusion kinetics of Zn^{2+} in AQ-VO and $V_2O_5{\cdot}nH_2O$. The GITT curves of AQ-VO and $V_2O_5{\cdot}nH_2O$ at 0.05 A g^{-1} are shown in **Fig. S14h** and **Fig. S14i**, respectively. As shown in **Fig. S14j**, the Zn^{2+} diffusion coefficients ($D_{Zn^{2+}}$: ca. 10^{-9}~10^{-10} cm^2 s^{-1}) in AQ-VO are obviously higher than those in $V_2O_5{\cdot}nH_2O$, indicating the more rapid ion transportation in AQ-VO, which may be stemmed from the pre-insertion of organic species to boost the diffusion of Zn^{2+}.

The electrochemical impedance spectra (EIS) of the samples have also been measured. **Fig. S14k** shows their Nyquist plots and the simulated equivalent circuit model, which consists of solution resistance (R_s), charge-transfer impedance (R_{ct}), constant phase element (CPE), and Warburg impedance (W). The fitted values for the equivalent circuit model are shown in **Table S2**. It can be seen that the R_{ct} at the AQ-VO electrode (7.99 Ω cm^{-2}) is obviously lower than that at the $V_2O_5{\cdot}nH_2O$ electrode

(29.6 Ω cm^{-2}), indicating more fast charge transfer at the AQ-inserted vanadium oxide. Furthermore, the R_{ct} at AQ-VO in the electrolyte with Al^{3+} (3.30 Ω cm^{-2}) is lower than that in the absence of Al^{3+} (7.99 Ω cm^{-2}), proving the presence of Al^{3+} can accelerate the charge transfer kinetics and improve the rate performance.

Table S2 The parameters in the equivalent circuit for AQ-VO and $V_2O_5 \cdot nH_2O$.

Sample/Electrolyte		R_s (Ω cm^{-2})	R_{ct} (Ω cm^{-2})	CPE	W (Ω cm^{-2})
AQ-VO	$Zn^{2+} + Al^{3+}$	1.22	3.30	6.6×10^{-3}	14.6
	Zn^{2+}	0.68	7.99	3.6×10^{-2}	25.09
$V_2O_5 \cdot nH_2O$	Zn^{2+}	1.21	29.6	1.2×10^{-2}	0.28

S5 *Ex situ* XRD patterns, SEM and EDS as well as elemental mappings of AQ-VO in 3 M $Zn(CF_3SO_3)_2$

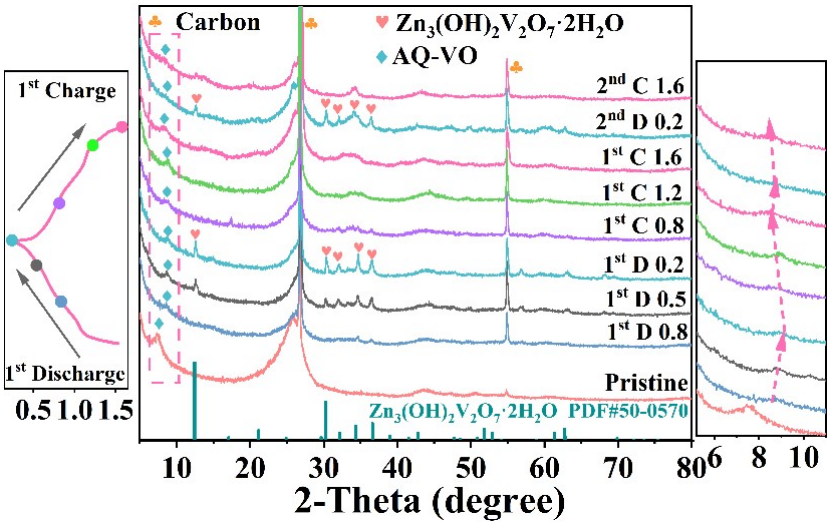

Fig. S15 *Ex situ* XRD patterns of the AQ-VO electrode in 3 M $Zn(CF_3SO_3)_2$

As shown in **Fig. S15**, in 3 M $Zn(CF_3SO_3)_2$, the (001) reflection peak slightly positively shifts during the discharge process, indicating the contraction of the interlayer spacing owing to the intercalation of Zn^{2+}. Meanwhile, new characteristic peaks ascribed to those of $Zn_3(OH)_2V_2O_7 \cdot 2H_2O$ (PDF#50-0570) were detected in the

discharge process, which can be attributed to the intercalated Zn^{2+} bonded with V–O layer. Subsequently, the $Zn_3(OH)_2V_2O_7{\cdot}2H_2O$ phase gradually disappears during the charge process, suggesting the recovery of the AQ-VO electrode. Similar phenomenon is observed in the 2nd cycle, suggesting the satisfactory reversibility of AQ-VO.

The SEM images of the pristine AQ-VO electrode are shown in **Fig. S16 (a, b)**, in which the microparticles and microsheets are the conducting agents of acetylene black and graphite, respectively. The F and N elements in the EDS spectrum come from the PVDF binder and NMP (**Fig. S16c** and **Table S3**), respectively. Upon the 1st discharge to 0.2 V in 3 M $Zn(CF_3SO_3)_2$, rose-like microsheets are observed on the surface of the AQ-VO electrode (**Fig. S16d, e**), which correspond to the new-generated $Zn_3(OH)_2V_2O_7{\cdot}2H_2O$ phase. And the Zn content is increased to 3.94 at. % with the intercalation of Zn^{2+} (**Fig. S16f** and **Table S3**). Upon the subsequent charge to 1.6 V, the rose-like microsheets vanish (**Fig. S16g, h**) with the Zn amount decreased to 2.56 at. % (**Fig. S16i** and **Table S3**), suggesting the partial recovery of the AQ-VO electrode.

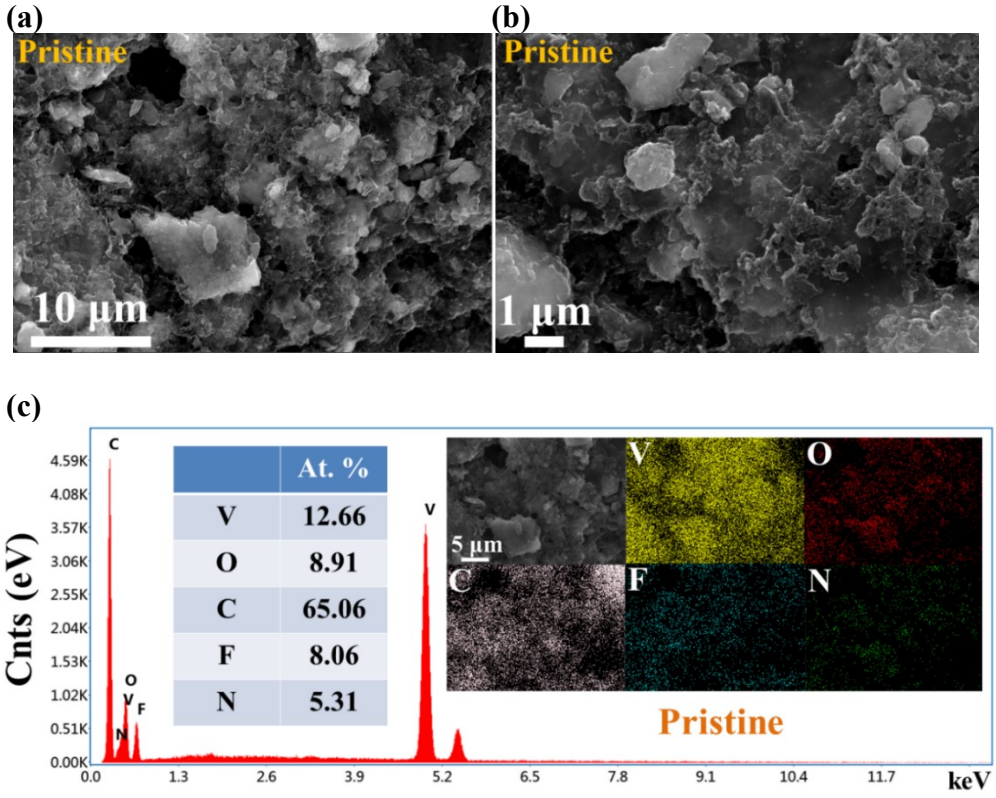

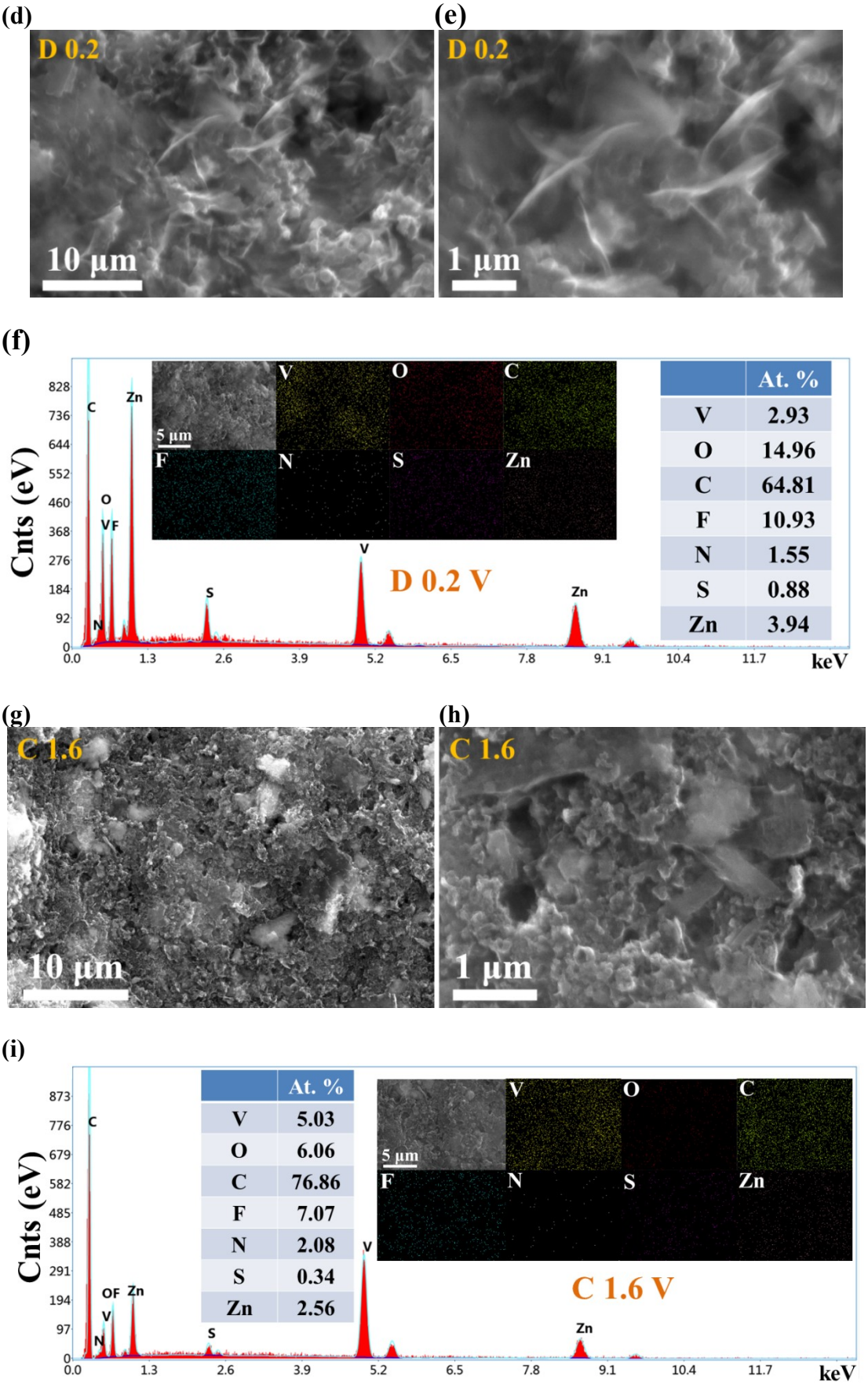

Fig. S16 (**a, b, d, e, g, h**) *Ex situ* SEM, (**c, f, i**) EDS as well as elemental mappings of

the AQ-VO electrode in 3 M $Zn(CF_3SO_3)_2$ during the 1st discharge and charge process, including (**a-c**) the pristine electrode, (**d-f**) discharge to 0.2 V (D 0.2) and (**g-i**) charge to 1.6 V (C 1.6).

Table S3 Element contents (at.%) of the AQ-VO electrode in the electrolytes with and without Al^{3+} under different states

At. %	**Pristine**	**1st D 0.2**	**1st C 1.6**	**1st D 0.2 with Al^{3+}**	**1st C 1.6 with Al^{3+}**
Al	/	/	/	1.05	0.56
V	12.66	2.93	5.03	3.18	2.23
O	8.91	14.96	6.06	11.63	15.28
C	65.06	64.81	76.86	70.58	69.53
F	8.06	10.93	7.07	7.12	8.14
N	5.31	1.55	2.08	3.70	2.46
S	/	0.88	0.34	0.48	0.82
Zn	/	3.94	2.56	2.26	0.98

S6 *Ex situ* SEM and EDS as well as elemental mappings of AQ-VO in the electrolyte of 2.8 M $Zn(CF_3SO_3)_2$ and 0.1 M $Al_2(SO_4)_3$

In the electrolyte of 2.8 M $Zn(CF_3SO_3)_2$ and 0.1 M $Al_2(SO_4)_3$, whether at the 1st fully discharged (D 0.2) or charge states (C 1.6), the AQ-VO electrode shows similar morphology (**Fig. S17a, b, d, e**) , agreeing with the fact that no new phase is formed during the discharge and charge process. The Zn content is increased to 2.26 at. % upon discharge to 0.2 V (**Fig. S17c**) and dropped to 0.98 at. % with the deintercalation of Zn^{2+} when charge to 1.6 V (**Fig. S17f**). The lower Zn residue at the fully charged state (0.98 at. %) suggests the better reversibility of the AQ-VO electrode in the electrolyte with Al^{3+} (**Table S3**).

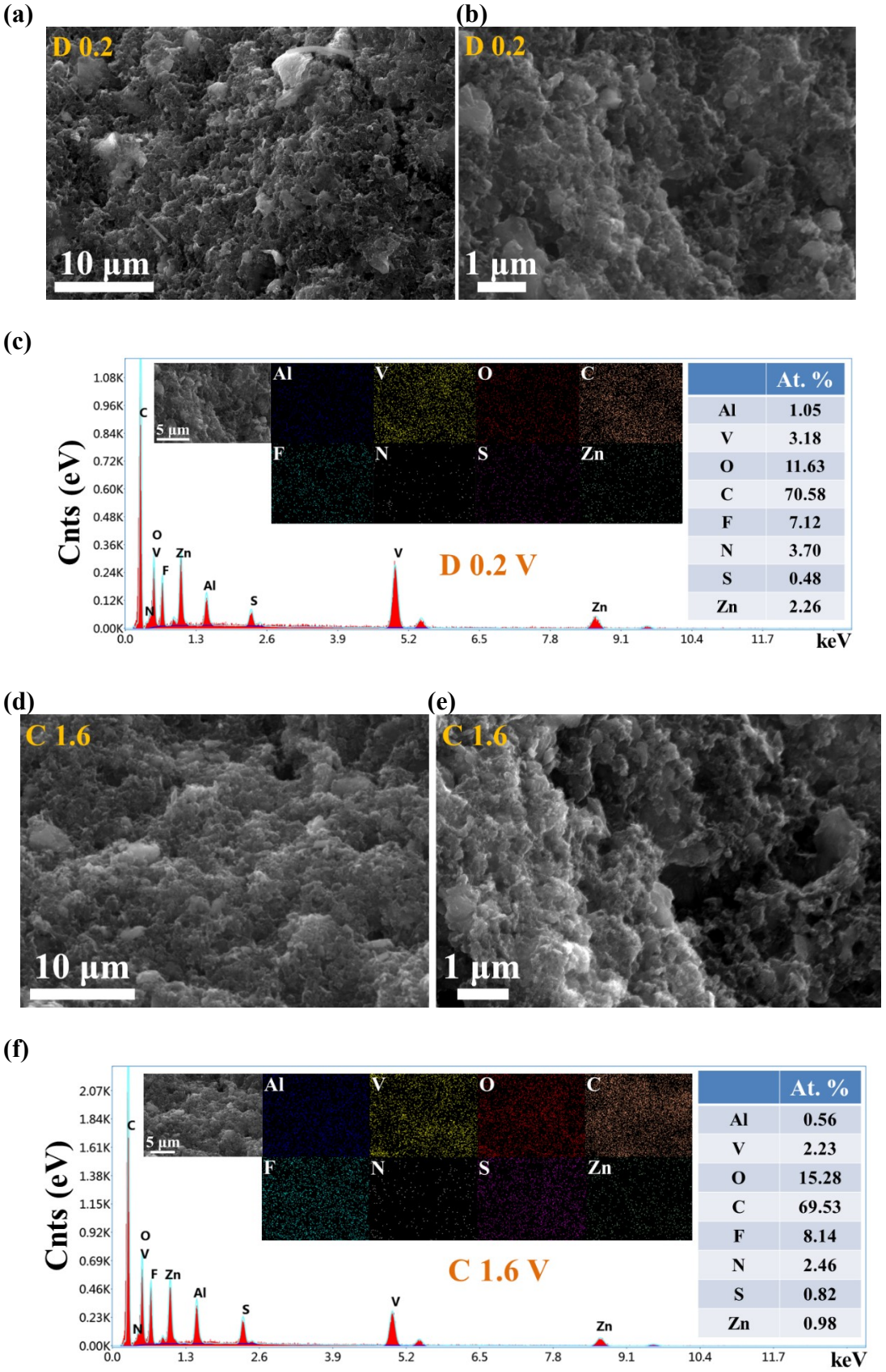

Fig. S17 *Ex situ* (**a, b, d, e**) SEM and (**c, f**) EDS as well as elemental mappings of the AQ-VO electrode in the electrolyte of 2.8 M $Zn(CF_3SO_3)_2$ and 0.1 M $Al_2(SO_4)_3$: (**a-c**) 1st discharge to 0.2 V and (**d-f**) charge to 1.6 V.

S7 *Ex situ* IR spectra of the AQ-VO electrode in 3 M $Zn(CF_3SO_3)_2$

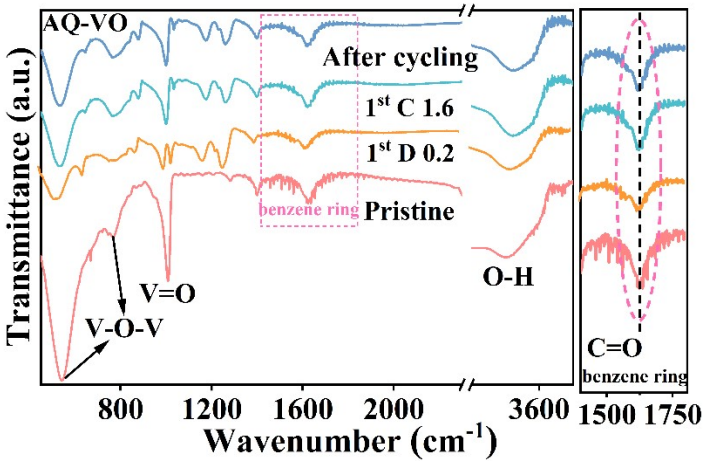

Fig. S18 *Ex situ* IR spectra of the AQ-VO electrode in the 3 M $Zn(CF_3SO_3)_2$ electrolyte.

As shown in **Fig. S18**, the IR peaks of the phenyl group (1400~ 1800 cm^{-1}) can be seen in the 1st fully discharged and charged AQ-VO electrode.[15] And the presence of C-O (~ 1150 cm^{-1}) and C=O (~ 1620 cm^{-1}) derives from the redox of C=O + e^- ↔ C-O.[15] Similar IR peaks of the AQ species are observed in the cycled AQ-VO electrode (Fig. S18), suggesting the maintenance of the organic species in AQ-VO in the discharge and charge cycles.

S8 *Ex situ* XPS of the AQ-VO electrode in 3 M $Zn(CF_3SO_3)_2$

Ex situ XPS of the AQ-VO electrode in 3 M $Zn(CF_3SO_3)_2$ have been measured. As shown in the **Fig. S19a**, the peaks located at 516.2 and 517.5 eV are assigned to V^{4+} $2p_{3/2}$ and V^{5+} $2p_{3/2}$ species, respectively. And the peaks at 523.4 and 524.9 eV are indexed to V^{4+} $2p_{1/2}$ and V^{5+} $2p_{1/2}$, respectively. When discharged to 0.2 V, the V^{4+} signal intensifies strongly along with the weakly of V^{5+} signal, suggesting that the partial reduction of the valence from V^{5+} to V^{4+} based on the electrochemistry. The charge process is reverse, indicating the oxidization of V^{4+}→V^{5+} during the process of

Zn^{2+} escape from V-O interlamination. In the O 1s XPS fine spectra (**Fig. S19b**), the pristine AQ-VO electrode exhibits five peaks located at 530.2, 531.5, 531.9, 532.6 and 533.6 eV, which can be index to V-O, oxygen defect, C=O, C-O and H_2O, respectively. When first charged to 0.2 V, the relative intensity of C=O group becomes weaker with the C-O signal intensified, which can be attributed to the reduction reaction of C=O + e^- → C-O in the discharge process. Then their relative intensities recover during the charge process, indicating the encouraging reversibility of the AQ organic species. The C 1s fine spectra are presented in **Fig. S19c**, in which the variation tendencies of the C=O and C-O signals are consistent with those in the O 1s spectra. And the peak at 290.8 eV is ascribed to -CF signal from the PVDF binder.

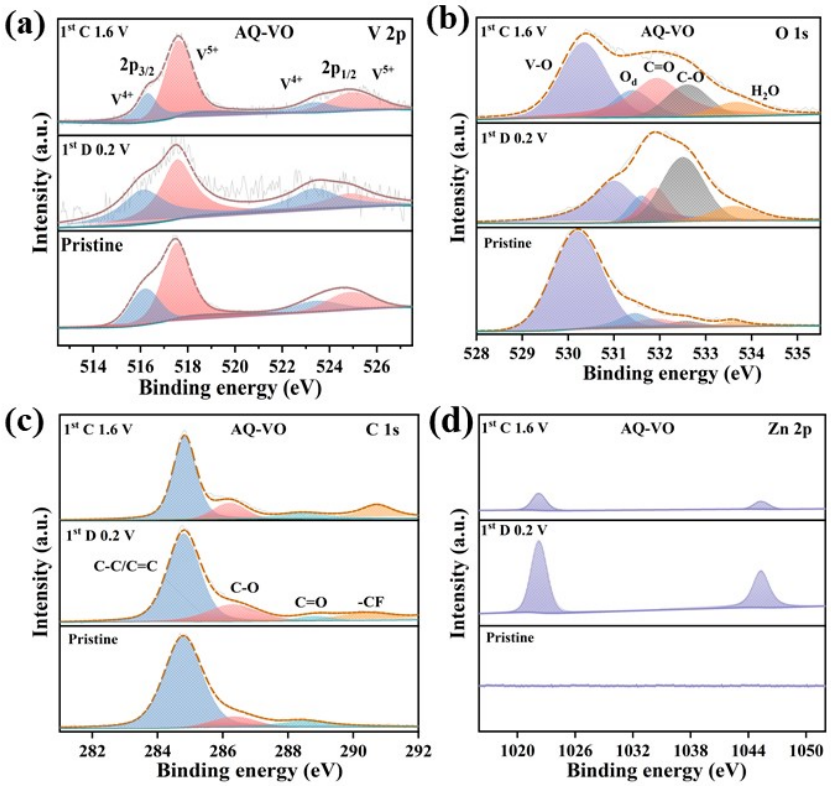

Fig. S19 *Ex situ* XPS spectra of the AQ-VO electrode in 3 M $Zn(CF_3SO_3)_2$ at different states: (**a**)V 2p, (**b**) O 1s, (**c**) C 1s, (**d**) Zn 2p.

Fig. S19d exhibits the Zn 2p spectra of the AQ-VO electrode at different states in the 1st cycle. No Zn signal is observed at the pristine state. When discharged to 0.2 V, the electrode shown two strong peaks at 1045.3 (Zn $2p_{1/2}$) and 1022.3 eV (Zn $2p_{3/2}$),

suggesting the successful insertion of Zn^{2+} ions into AQ-VO. When subsequently charged to 1.6 V, the Zn 2p signals become weaker remarkably, manifesting that most of the Zn^{2+} ions have escaped from AQ-VO.

S9 *Ex situ* XPS of the AQ-VO electrode in the electrolyte of 2.8 M $Zn(CF_3SO_3)_2$ and 0.1 M $Al_2(SO_4)_3$

As shown in **Fig. 4b**, with the intercalation of Zn^{2+} during the discharge process, V^{5+} is reduced into V^{4+}, the ratio of V^{4+}/V^{5+} is increased, whereas the charge process is on the contrary. The Al 2p fine spectra of the fully discharged and charged AQ-VO electrodes in the electrolyte with Al^{3+} show the Al 2p signal (**Fig. 4c**), further confirming that the intercalation of Al^{3+} into the AQ-VO electrode.

As displayed in **Fig. S20a**, the O 1s spectra in the electrolyte with and without Al^{3+} present similar variation trend during the 1st cycle. Moreover, the variation tendencies of the C 1s (**Fig. S20b**) and Zn 2p (**Fig. S20c**) fine spectra during the discharge and charge process in the electrolyte with Al^{3+} are similar to those in 3 M $Zn(CF_3SO_3)_2$.

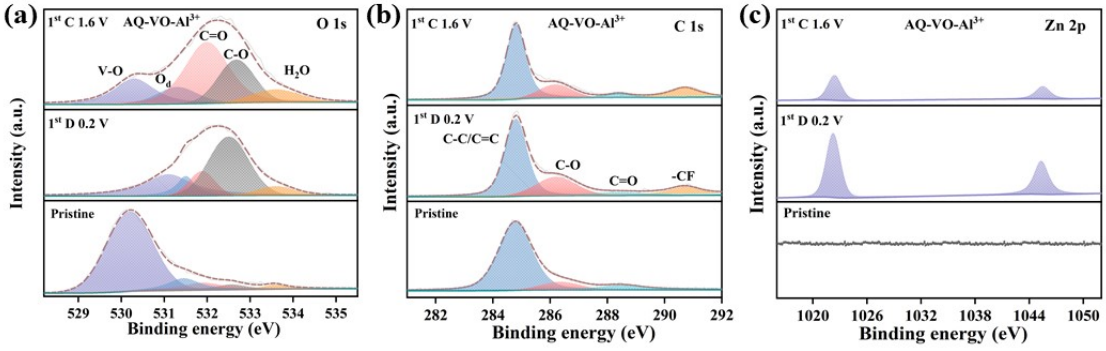

Fig. S20 *Ex situ* XPS spectra of the AQ-VO electrode in the electrolyte of 2.8 M $Zn(CF_3SO_3)_2$ and 0.1 M $Al_2(SO_4)_3$ at different states: (**a**) O 1s, (**b**) C 1s and (**c**) Zn 2p.

The interconversion of C=O ↔ C-O is also confirmed by *ex situ* XPS of the AQ-VO electrode in the electrolytes with and without Al^{3+}. In brief, whether in the absence or presence of Al^{3+}, with the occurrence of reduction reaction during the discharge

process, the molar ratio of C-O/C=O is increased (**Fig. S19b, c** and **Fig. S20a, b**). And the charge process is reverse.

In conclusion, by comparing the XPS results of AQ-VO electrode in the electrode without and with Al^{3+}, it is found that the Al^{3+} ions in the electrolyte have no obvious effect on the valence states of the other elements in the discharged and charged AQ-VO electrodes. However, the intercalated Al^{3+} can act as interlayer pillar in the inner channel of AQ-VO to expedite the diffusion kinetics and maintain the structural stability.

S10 The characterizations of the cycled AQ-VO electrodes in the electrolytes with and without Al^{3+}

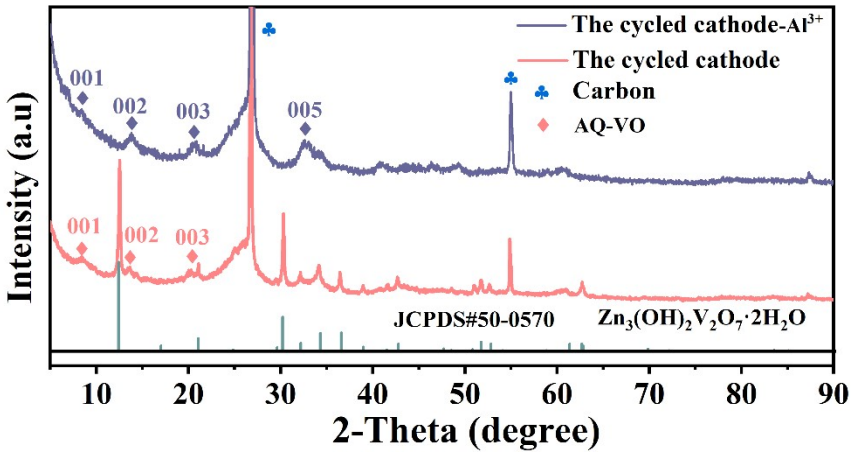

Fig. S21 XRD patterns of the AQ-VO electrodes in the electrolytes with and without Al^{3+} after the cycling test at 1 A g^{-1}.

Fig. S21 depicts the XRD patterns of the AQ-VO electrodes in the electrolytes with and without Al^{3+} after the cycling test at 1 A g^{-1}. As shown in **Fig. S21**, in the electrolyte with Al^{3+}, the cycled AQ-VO cathode maintains its characteristic (00*l*) reflection peaks such as (001), (002), (003) and (005), et al, indicating the structural stability of the AQ-VO sample in the Al^{3+} additive. It is due to the dual-pillar effect of the Al^{3+} and the AQ organic species, leading to the reversible (de)intercalation of Zn^{2+}. In comparison, in the electrolyte without Al^{3+}, apart from the characteristic peaks of AQ-VO, strong

diffraction signals of $Zn_3(OH)_2V_2O_7{\cdot}2H_2O$ (PDF#50-0570) are also observed in the XRD pattern of the cycled AQ-VO cathode, agreeing with the *ex-situ* XRD patterns upon the 1st and 2nd discharge process. The formation of $Zn_3(OH)_2V_2O_7{\cdot}2H_2O$ is probably associated with the partial irreversible intercalation of Zn^{2+}.

S11 The effect of the Al^{3+} additive in the electrolyte on the Zn anode

S11.1 The effect of the Al^{3+} additive in the electrolyte on the cycled Zn anode in the Zn||AQ-VO cell

The cycled Zn anodes in the Zn||AQ-VO cells with and without Al^{3+} additive have also been characterized. As shown in **Fig. S22a**, the XRD patterns of the cycled Zn anodes in the electrolytes with and without Al^{3+} are similar to that of the pristine Zn anode, they both exhibit three strong diffraction peaks at 42.5, 45.6, and 50.7 °, which are attributed to the (002), (100) and (101) crystalline planes of Zn (PDF: 87-0713), respectively. It should be mentioned that the relative intensities of these diffraction peaks in the pristine Zn foil and the cycled Zn anode without the Al^{3+} additive are similar. Among them, the (101) reflection peak displays the strongest intensity. This is also observed for other reported Zn anodes in zinc-ion batteries. Whereas for the cycled Zn anode in the electrolyte with Al^{3+}, the (002) peak is much stronger than the (100) and (101) peaks, indicating that the additive of Al^{3+} can promote the Zn deposition along the (002) facet. This growth can effectively inhibit the appearance of zinc dendrites, leading to a long-term cycle life.[16, 17]

(a)

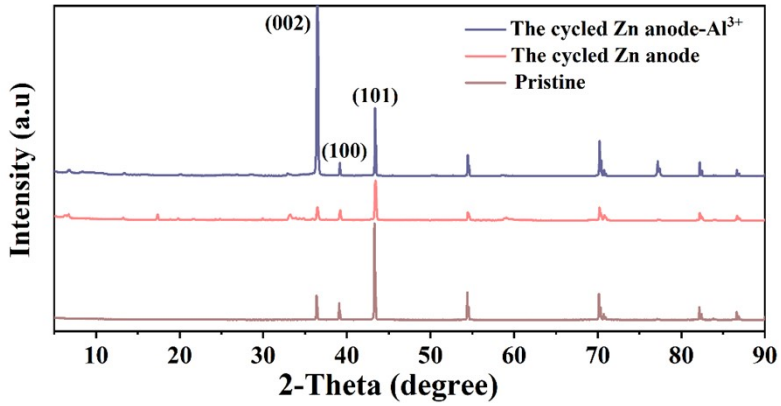

(b)

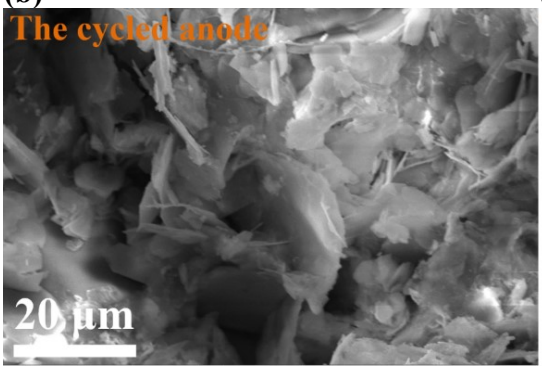

(c)

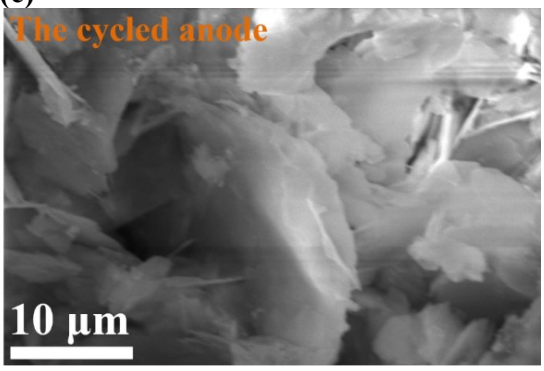

(d)

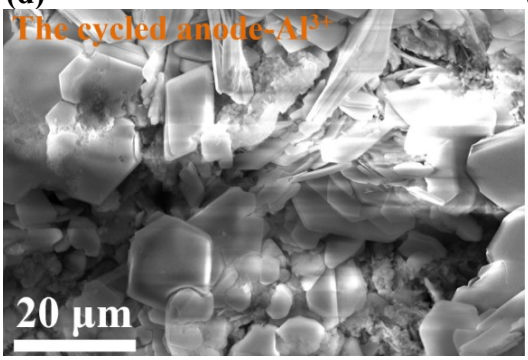

(e)

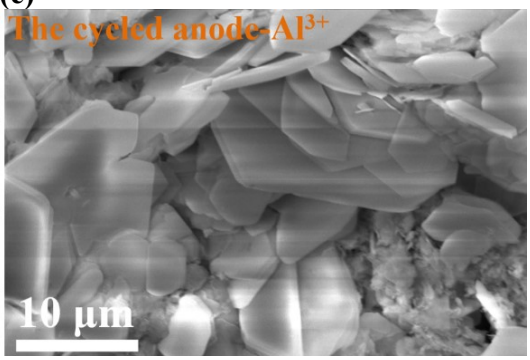

(f)

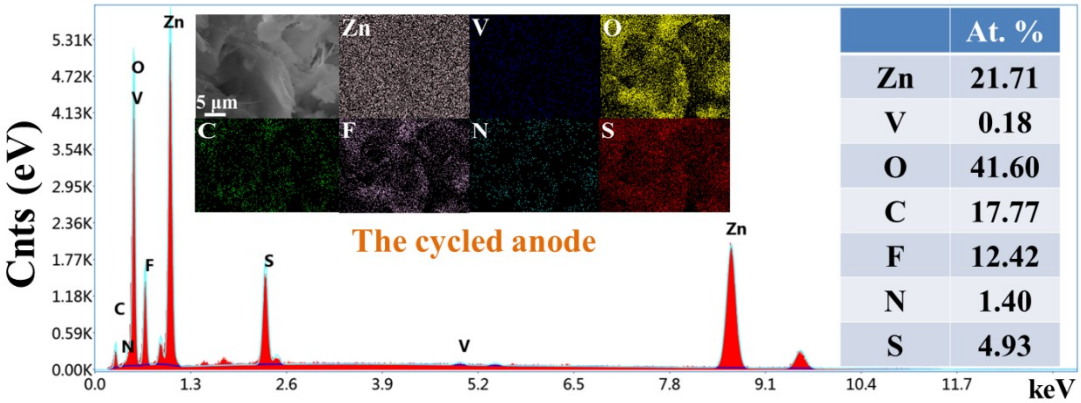

	At. %
Zn	21.71
V	0.18
O	41.60
C	17.77
F	12.42
N	1.40
S	4.93

(g)

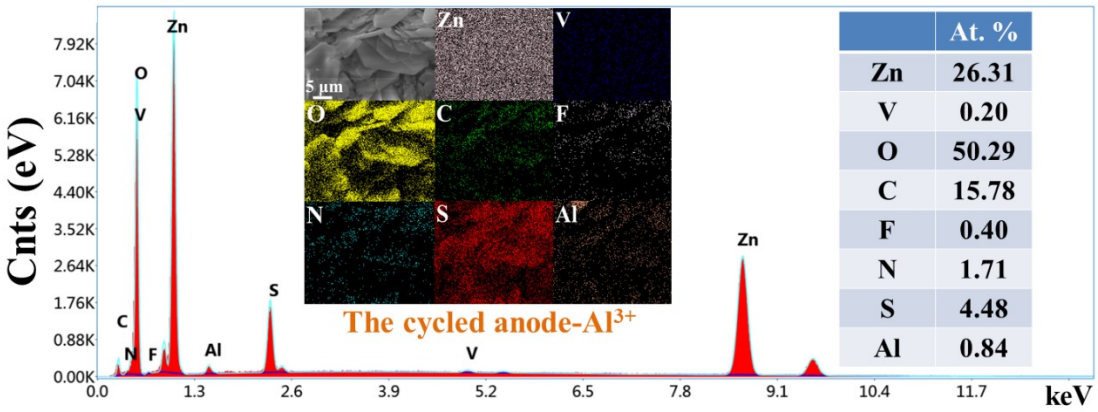

Fig. S22 (**a**) XRD patterns, (**b-e**) SEM images and (**f**, **g**) EDS as well as elemental mappings of the Zn anodes in the electrolytes (**b**, **c**, **f**) with and without (**d**, **e**, **g**) Al^{3+} after the cycling test at 1 A g^{-1}.

The expectation is also proved by their SEM images. As shown in **Fig. S22(b**, **c**), on the surface of the cycled Zn anode in the absence of Al^{3+}, loosely stacked flakes are observed, which are consistent with the dendritic products typically observed in an inhomogeneous Zn stripping/plating process. The continuous growth of the dendrites would eventually pierce through the separator to short the battery device. In contrast, in the electrolyte with Al^{3+}, the cycled Zn anode shows a much denser and flatter morphology like solid rock covered on the surface (**Fig. S22d**, **e**). Moreover, its EDS and elemental mappings detect the presence of Al on the surface of the cycled Zn anode (**Fig. S22g**), indicating that Al^{3+} has played an important role in the relatively homogeneous Zn deposition/dissolution process.

S11.2 The effect of the Al^{3+} additive in the electrolyte on the Zn anode in Zn||Zn symmetric cell

(a)

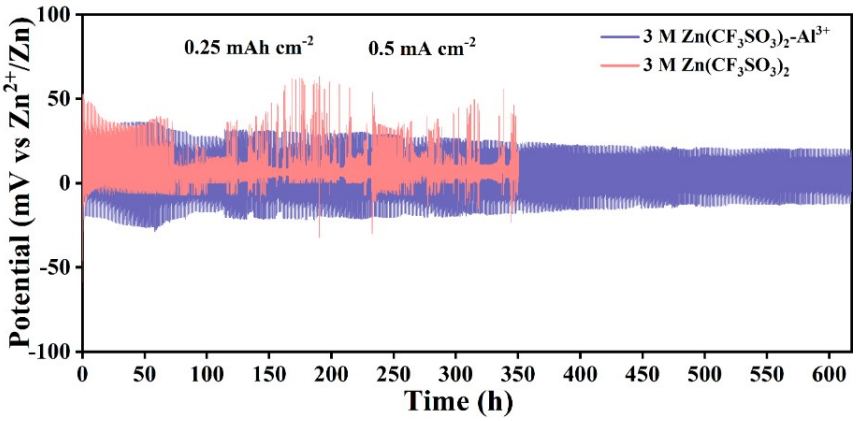

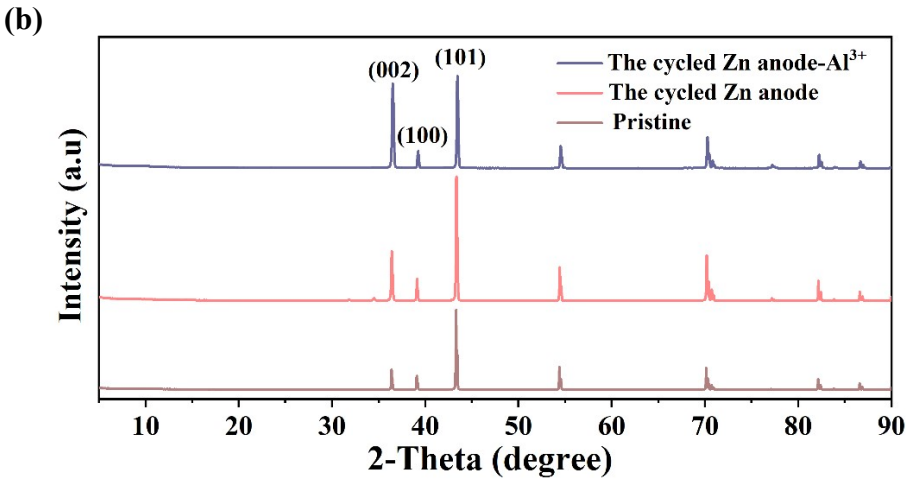

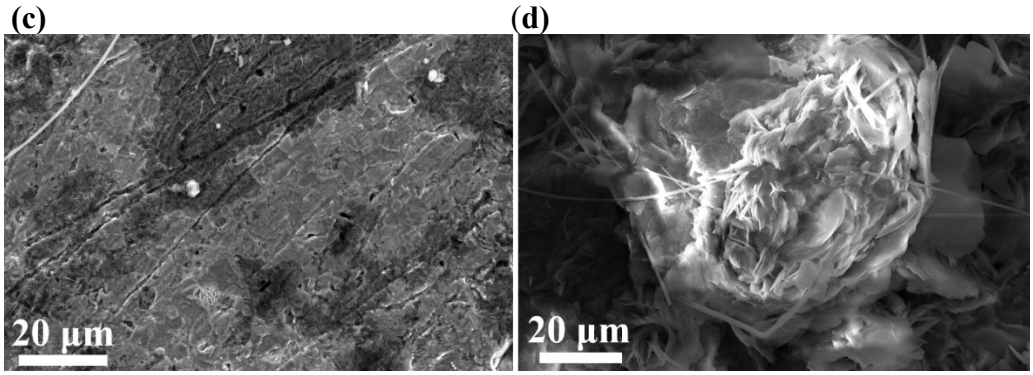

Fig. S23 (**a**) Cycling performances of the Zn//Zn symmetric cells at 0.5 mA cm^{-2} and 0.25 mAh cm^{-2} in different electrolytes; (**b**) XRD patterns and (**c**, **d**) SEM images of the Zn foils in the electrolytes (**c**) with and (**d**) without Al^{3+} after the cycling test.

To further verify the effect of the Al^{3+} additive on Zn metal, the cycling performances of the Zn//Zn symmetric cells in the electrolytes with and without Al^{3+} were performed at a current density of 0.5 mA cm^{-2} and an areal capacity of 0.25 mAh cm^{-2}. As shown in **Fig. S23a**, the symmetric Zn//Zn cell in the electrolyte of 2.8 M $Zn(CF_3SO_3)_2$ and 0.1 M $Al_2(SO_4)_3$ can discharge and charge steadily over 620 h. As a comparison, the Zn//Zn cell in the 3 M $Zn(CF_3SO_3)_2$ electrolyte shows a much short lifespan (75 h) due to short circuit, which may be caused by the dendrite growth. The XRD patterns of the cycled Zn foils in the electrolytes with and without Al^{3+} were carried out comparatively to investigate the effect of the Al^{3+} ions in the electrolyte on Zn metal. As displayed in **Fig. S23b**, the two cycled Zn foils both exhibit the (002), (100) and (101) crystalline planes of Zn (PDF: 87-0713). However, the relative intensity of the (002) peak in the XRD pattern of the cycled Zn foil in the electrolyte with Al^{3+} is much stronger than those in the pristine Zn foil and the cycled Zn foil in the electrolyte without Al^{3+}, indicating that the additive of Al^{3+} can promote the Zn deposition along the (002) facet, which can hinder the growth of zinc dendrites, resulting in a long-term cycle life.

The speculation is evidenced by the SEM images of the Zn foils after the cycling test. As shown in **Fig. S23c**, in the electrolyte with Al^{3+}, the surface of the cycled Zn foil is smooth and flat. In contrast, in the absence of Al^{3+}, obvious Zn dendrites can be observed on the surface of the cycled Zn foil (**Fig. S23d**). It may be due to the electrostatic shield effect, which is caused by the lower reduction potential of Al^{3+} (-1.622 V vs RHE).[18]

In summary, whether in the Zn||Zn symmetric cell or Zn||AQ-VO cell, the Al^{3+} additive in the electrolyte can achieve a uniform nucleation/deposition to suppress the growth of Zn dendrites on the Zn foil.

S12 The binding energies and configurations of Zn^{2+} intercalated on some sites in the inner channel of AQ-VO

In order to reveal the reason for the formation of $Zn_3(OH)_2V_2O_7{\cdot}2H_2O$ when AQ-VO is fully discharged in 3 M $Zn(CF_3SO_3)_2$, DFT calculations were performed. As shown in **Fig. S24a**, when Zn^{2+} is intercalated on site I in the inner channel of AQ-VO, Zn^{2+} is coordinated with three oxygen atoms from one V-O-V monolayer and one oxygen atom from the lattice water molecule (Zn-O distances: 1.897 ~ 2.162 Å) to furnish a distorted tetrahedral geometry with a binding energy of -2.21 eV. And when Zn^{2+} is intercalated on site II, Zn^{2+} almost shows a planar square environment, which is coordinated with two neighboring quinonyl groups from one AQ and two oxygen atoms from one V-O-V monolayer (Zn-O distances: 1.905 ~ 2.008 Å) with a binding energy of -1.72 eV (**Fig. 24b**). The negative binding energy indicates that the intercalation of Zn^{2+} on sites I and II in the inner channel of AQ-VO is thermally stable, which probably can lead to the formation of $Zn_3(OH)_2V_2O_7{\cdot}2H_2O$.[10, 19, 20 21]

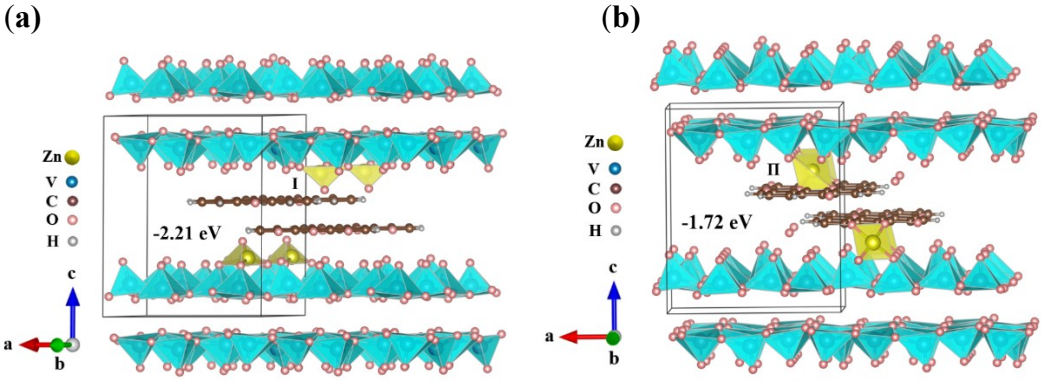

Fig. S24 The configurations of the Zn^{2+} intercalated on sites (**a**) I and (**b**) II in the inner channel of AQ-VO.

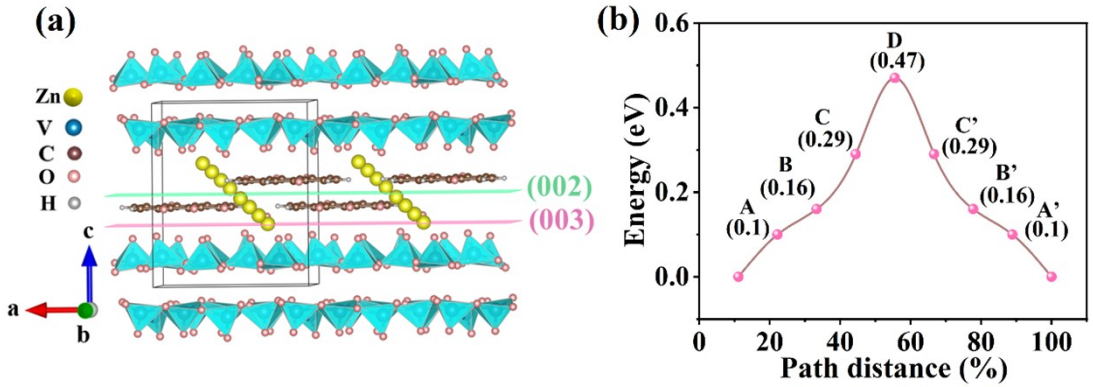

Fig. S25 (**a**) Schematic illustration of the diffusion path of Zn^{2+} in AQ-VO; (**b**) The corresponding energy profile for Zn^{2+} across each site.

Climbing image-nudged elastic band (CI-NEB) method was also utilized to calculate the Zn^{2+} diffusion path and barrier in AQ-VO. As shown in **Fig. S25b** and **Fig. S26**, Zn^{2+} migrates across sites A→ B→ C→ D→ C'→ B'→ A' (A'-C' are the symmetrical sites of A-C) with a small energy barrier of 0.47 eV, which can explain the fast Zn^{2+} diffusion kinetics in AQ-VO. Moreover, it can be seen that the Zn^{2+} diffusion path crosses the (002) and (003) facets (**Fig. S25a**), which probably can account for the dynamic conversion between disorder and order on the (00*l*) facets during the discharge and charge process.

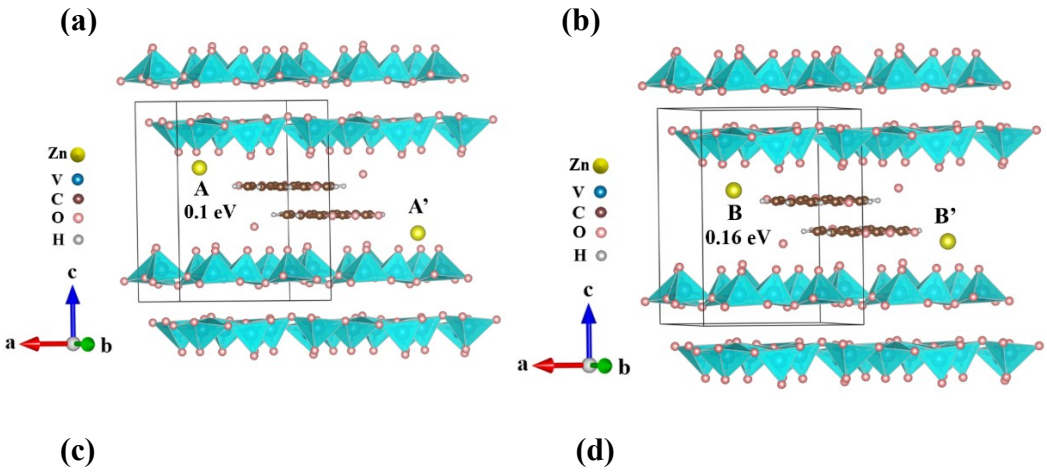

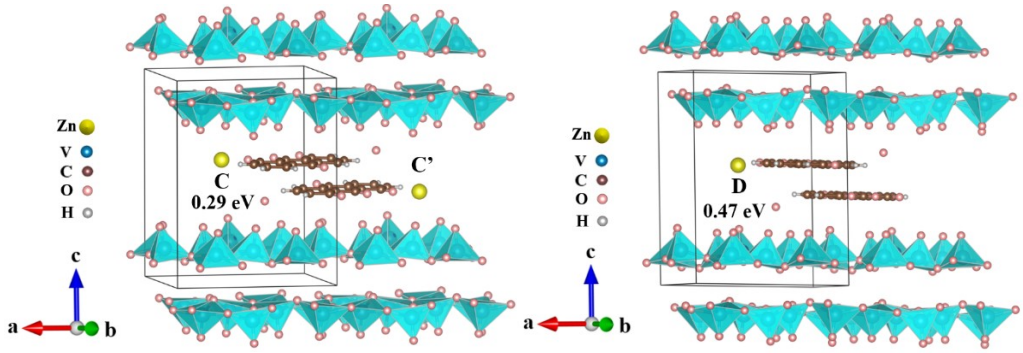

Fig. S26 The optimized configurations of Zn^{2+} intercalated on sites (**a**) **A** (**A'**), (**b**) **B** (B'), (**c**) **A** (**A'**) and (**d**) **D** in the inner channel of AQ-VO.

References:

1. G. Kresse and J. Furthmüller, *Comput. Mater. Sci.*, 1996, **6**, 15-50.
2. J. P. Perdew, K. Burke and M. Ernzerhof, *Phys. Rev. Lett.*, 1996, **77**, 3865-3868.
3. J. Behler, *J. Chem. Phys.*, 2011, **134**, 074106.
4. R. Nadimicherla, Y. Liu, K. Chen and W. Chen, *Microelectron. Eng.*, 2014, **127**, 81-85.
5. X. Wang, B. Xi, X. Ma, Z. Feng, Y. Jia, J. Feng, Y. Qian and S. Xiong, *Nano Lett.*, 2020, **20**, 2899-2906.
6. J. Li, K. McColl, X. Lu, S. Sathasivam, H. Dong, L. Kang, Z. Li, S. Zhao, A. G. Kafizas, R. Wang, D. J. L. Brett, P. R. Shearing, F. Corà, G. He, C. J. Carmalt and I. P. Parkin, 2020, **10**, 2000058.
7. C. Liu, Z. Neale, J. Zheng, X. Jia, J. Huang, M. Yan, M. Tian, M. Wang, J. Yang and G. Cao, *Energy Environ. Sci.*, 2019, **12**, 2273-2285.
8. Y. Yang, Y. Tang, G. Fang, L. Shan, J. Guo, W. Zhang, C. Wang, L. Wang, J. Zhou and S. Liang, *Energy Environ. Sci.*, 2018, **11**, 3157-3162.
9. F. Ming, H. Liang, Y. Lei, S. Kandambeth, M. Eddaoudi and H. N. Alshareef, *ACS Energy Lett.*, 2018, **3**, 2602-2609.
10. Y. Liu, X. Xiao, X. Liu, L. L. Cui and Y. Gong, *J. Mater. Chem. A*, 2022, **10**, 912-927.
11. L. Hu, Z. Wu, C. Lu, F. Ye, Q. Liu and Z. Sun, *Energy Environ. Sci.*, 2021, **14**, 4095-4106.
12. D. Bin, W. Huo, Y. Yuan, J. Huang, Y. Liu, Y. Zhang, F. Dong, Y. Wang and Y. Xia, *Chem*, 2020, **6**, 968-984.
13. Z. Wu, C. Lu, F. Ye, L. Zhang, L. Jiang, Q. Liu, H. Dong, Z. Sun and L. Hu, *Adv. Funct. Mater.*, 2021, **31**, 2106816.
14. Q. Zong, Q. Wang, C. Liu, D. Tao, J. Wang, J. Zhang, H. Du, J. Chen, Q. Zhang and G. Cao, *ACS Nano*, 2022, **16**, 4588-4598.
15. Y. Gao, G. Li, F. Wang, J. Chu, P. Yu, B. Wang, H. Zhan and Z. Song, *Energy Storage Mater.*, 2021, **40**, 31-40.
16. Y. Liu, J. Hu, Q. Lu, M. Hantusch, H. Zhang, Z. Qu, H. Tang, H. Dong, O. G. Schmidt, R. Holze and M. Zhu, *Energy Storage Mater.*, 2022, **47**, 98-104.
17. W. Du, J. Yan, C. Cao and C. C. Li, *Energy Storage Mater.*, 2022, **52**, 329-354.
18. P. Wang, X. Xie, Z. Xing, X. Chen, G. Fang, B. Lu, J. Zhou, S. Liang and H. J. Fan, *Adv. Energy*

Mater., 2021, **11**, 2101158.
19. W. Leng, X. Liu and Y. Gong, *Chem. Eng. J.*, 2022, **431**, 134034.
20. X. Liu, T. Cao, S. Li, Y. Liu, Y. Gong and D. Zhang, *J. Power Sources*, 2022, **525**, 231134.
21. Y. Liu, J. Lv, T. Cao, Y. Gong and D. Zhang, *Chem. Eng. J.*, 2022, **441**, 136007.